Applied Surface Science 732 (2026) 166536

Contents lists available at ScienceDirect

Applied Surface Science

journal homepage: www.elsevier.com/locate/apsusc

Full Length Article

Harnessing oxygen electrocatalysis through exsolved Pt nanoparticles from $La_{0.6}Sr_{0.4}Fe_{0.95}Pt_{0.05}O_{3-\delta}$

Anna Paola Panunzi [a], Leonardo Duranti [a], Elisabetta Di Bartolomeo [a], Jinzhen Huang [b], Camelia N. Borca [c], Thomas Huthwelker [c], Dominika Baster [b], Mario El Kazzi [b], Marcello Marelli [d], Emiliana Fabbri [b,*], Juliana Bruneli Falqueto [b,*]

[a] Department of Chemical Science and Technologies, University of Rome Tor Vergata, Via della Ricerca Scientifica, 00133 Rome, Italy
[b] PSI Center for Energy and Environmental Science, 5232 Villigen PSI, Switzerland
[c] PSI Center for Photon Science, 5232 Villigen PSI, Switzerland
[d] CNR SCITEC - Istituto di Scienze e Tecnologie Chimiche "Giulio Natta", Via Fantoli 16/15, 20138 Milano, Italy

ARTICLE INFO

Keywords:
Pt exsolution
Distribution of relaxation times DRT
Perovskite
Oxygen evolution reaction OER
Oxygen reduction reaction ORR

ABSTRACT

This work explores the exsolution of well-dispersed nanoparticles containing reduced Pt species from $La_{0.6}Sr_{0.4}Fe_{0.95}Pt_{0.05}O_{3-\delta}$ (LSFPt) as an effective approach to design catalysts for oxygen electrocatalysis. A 10 h reduction treatment at 500 °C in 5% H_2/Ar promotes the exsolution of ~1.2 nm Pt nanoparticles on the surface, increasing oxygen deficiency without compromising the perovskite structure. The resulting catalyst exhibits over 2.5-fold performance improvement for oxygen evolution reaction (OER) and reduction reaction (ORR) in alkaline media compared to the as-prepared LSFPt. Specifically, OER potential decreased from 1.61 to 1.58 V_{RHE}, while the ORR potential improved from 0.31 to 0.48 V_{RHE}. Electrochemical impedance spectroscopy (EIS), combined with distribution of relaxation times (DRT) deconvolution analysis, revealed a notable decrease in medium-frequency resistance, indicating enhanced charge transfer at the electrode surface for OER and ORR. *Post-mortem* O K-edge spectra obtained by soft X-ray absorption spectroscopy in total electron yield mode further suggest an increased surface restructuring in the reduced LSFPt, attributed to the synergistic presence of surface defects and exsolved nanoparticles containing reduced Pt species. This one-step reduction protocol provides a valuable methodological insight for designing catalysts for oxygen electrocatalysis by tailoring the surface composition of perovskite material aligned with the necessity for bifunctional systems.

1. Introduction

In the current energy scenario, implementing innovative technologies is crucial for the transition towards clean and renewable energy sources. Developing efficient energy storage and conversion systems is essential to compensate for the intermittent nature of renewable energy sources and to facilitate the replacement of fossil fuels. Low-temperature alkaline fuel cells and electrolyzers are energy conversion technologies capable of converting energy by the reduction/oxidation reaction at the electrodes [1,2]. Unified regenerative fuel cells (URFC) integrate both fuel cell (gas-to-power) and electrolyzer (power-to-gas) into a single device, allowing switching between the two modes as needed [3]. This dual functionality offers significant advantages for commercialization by enabling a simplified, integrated system. While the cost-saving benefits of a URFC are most pronounced in acidic systems (which use precious-metal-based catalysts), their value for alkaline systems (which use more affordable catalysts) are not eliminated but are instead shifted to the system's simplification and operational levels. A single URFC unit dramatically reduces the size, weight, and complexity of the overall energy system by combining the functions of an electrolyzer and fuel cell into one stack. This is particularly crucial for applications requiring a compact space, such as portable power, military equipment, and aerospace. Furthermore, this integrated design reduces the number of redundant auxiliary components, including pumps, valves, and control systems, which lowers the capital and maintenance costs and decreases the number of potential points of failure [4]. One of the major challenges in large-scale URFC is developing stable and efficient electrocatalyst materials for the oxygen electrode. These materials must simultaneously provide catalytically active sites for the oxygen reduction reaction (ORR) and for the oxygen evolution reaction (OER), while maintaining

* Corresponding authors.
E-mail addresses: emiliana.fabbri@psi.ch (E. Fabbri), juliana.bruneli-falqueto@psi.ch (J.B. Falqueto).

https://doi.org/10.1016/j.apsusc.2026.166536
Received 9 November 2025; Received in revised form 4 March 2026; Accepted 5 March 2026
Available online 7 March 2026

stability across a wide potential range. The ORR and the OER are kinetically sluggish electrochemical reactions with high overpotentials, which significantly affect the performance of the fuel cell and electrolyzer. [5]. Currently, NiFe (oxy)hydroxides for OER and metal-based materials (both noble, such as Pt, and non-precious, such as Ag) for ORR are state-of-the-art electrocatalysts for oxygen reaction electrodes in alkaline media [6–8]. However, while these electrocatalysts exhibit high activity for either ORR or OER, none possess the bifunctionality required for both reactions in URFC applications. Therefore, developing new classes of electrocatalysts with high activity for both oxygen electrochemical reactions remains an open challenge, driving significant research efforts.

Transition metal oxides have been extensively studied as bifunctional materials with high activity for both OER and ORR [9]. Perovskite oxides (ABO_3) have attracted significant interest as electrocatalysts due to their unique structural and electronic properties [5,10,11]. Their application is well established in the development of high-temperature reversible solid oxide cells (r-SOCs) [12,13]; however, in recent decades, they have also been extensively investigated as oxygen electrodes for low-temperature alkaline fuel cells and electrolyzers [14,15]. The electrocatalytic activity of perovskites can be easily tuned by changing different parameters, such as the number of *3d* electrons and spin state in the B-site transition metals (TM), covalency of TM *3d*-O*2p* bonds, and oxygen vacancy content [16–18]. In this context, the composition of both A- and B-sites can be modified to tailor perovskite-based materials with specific properties, enabling the development of highly efficient and versatile electrocatalysts for both OER and ORR.

Lanthanum iron oxide, $LaFeO_3$, exhibits a perovskite-like structure that is widely used in high-temperature solid oxide applications. Recently, there have been studies of $LaFeO_3$ also for low-temperature applications. Their catalytic activity toward oxygen reactions in alkaline media can be easily enhanced by both A- and B-site modifications. For example, the partial substitution of La^{3+} cations with Sr^{2+} at the A-site has been reported to enhance the activity towards OER due to the formation of oxygen vacancies in the structure [19,20]. In addition, the partial B-site substitution with different metal cations can improve $LaFeO_3$ electrochemical performances by modifying the electronic state of the perovskite [21,22]. $LaFeO_3$-based structures can also be successfully used as support for metal nanoparticles. It has also been reported that $LaFeO_3$ perovskites can easily change their structure when treated at high temperatures (up to 300 °C) and reducing conditions. This heat treatment triggers the migration of the B-site metal ions from the bulk to the surface, consequently forming a uniform metallic nanoparticles layer, in a process called exsolution [23–25]. This method, with respect to other impregnation/decoration methods, allows for well-anchored nanoparticles within the perovskite substrate with a better control of size and shape, leading to improved electrochemical performance [26–28]. This method enables the co-existence of exsolved nanoparticles on the catalyst surface, which can act as active sites for both oxygen reactions, along with a stable perovskite substrate. The use of temperature-controlled reduction treatment to trigger metal exsolution has been commonly used for high-temperature solid oxide fuel electrode applications, and only recently employed to boost the performance of oxygen electrodes for low-temperature alkaline applications [29–31]. For example, Ni-exsolution from lanthanum-based perovskite was proved to be a successful strategy to achieve high OER activity in alkaline environments [29,30]. Also, promising bifunctional OER/ORR performance has been reported by the formation of exsolved Co-Fe bimetallic nanoparticles on a lanthanum ferrite perovskite surface [31,32]. These examples suggest a promising strategy for developing efficient bifunctional catalysts: doping the B-site of a promising OER perovskite catalyst with noble metals (*e.g.*, Pt, Pd, Ru). Despite their high costs, noble metals demonstrate high reducibility and an energetically favored exsolution process with respect to other metals [23,33]. This feature allows the use of a very small amount of metal as a B-site dopant with high nanoparticle exsolution rates. Platinum's effectiveness as an ORR catalyst is well-established, and the use of exsolved Pt metal nanoparticles to promote the catalytic activity toward different fuel electrode reactions, such as H_2 oxidation and CO_2 reduction, has been recently assessed in reversible solid oxide cell systems for high-temperature applications [34–36]. Recent researches have highlighted the efficacy of exsolution of Pt from La-based perovskite structures in promoting OER and OER/HER activity in low-temperature alkaline environments [37,38]. Low-level Pt doping (0.5%) in $LaAlO_3$ has been shown to trigger the exsolution of ultra-small nanoparticles of 1–2 nm, significantly boosting ORR activity and stability in alkaline media [37]. Similarly, Pt exsolution from $LaCoO_3$ has been achieved at a low temperature of 350 °C, enhancing OER performance by optimizing oxygen vacancies and promoting synergistic metal-support interactions [38]. Despite these advancements, these studies often focus on a single catalytic direction or utilize host lattices with limited intrinsic bifunctionality. Additionally, the investigation of the role of surface modification and Pt nanoparticle exsolution via reduction treatment remains a significant challenge and it is not fully elucidated.

In this work, the exsolution of Pt nanoparticles from $La_{0.6}Sr_{0.4}Fe_{0.95}Pt_{0.05}O_{3-\delta}$ (LSFPt) is evaluated as a promising strategy to improve oxygen reactions. Two perovskite samples were investigated: the as-prepared LSFPt, and the reduced LSFPt, where Pt was exsolved onto the surface via a reduction heat treatment. The high reducibility of Pt ions allows the formation of defined Pt nanoparticles on the perovskite surface by choosing the proper reduction temperature treatment. At the same time, the possibility of having high coverage of metallic nanoparticles at less harsh temperature conditions is crucial for enhancing the oxygen deficiency on the catalyst surface while preserving the perovskite structure. During the reduction treatment, Pt incorporated into the perovskite lattice migrates toward the surface, forming nanoparticles containing reduced Pt species. This transformation results in a catalyst with both oxygen defects and exsolved Pt-based nanoparticles. The synergistic effect of the defective surface from the host perovskite and the exsolved Pt nanoparticles offers a methodological insight towards designing catalysts for oxygen electrocatalysis. The structure and morphology of the as-prepared and reduced LSFPt materials were characterized using X-ray powder diffraction (XRPD), thermogravimetric analysis (TGA), X-ray photoelectron spectroscopy (XPS), and transmission electron microscopy (TEM). The electrochemical activity towards both OER and ORR in alkaline media was evaluated to highlight the beneficial effects of the structural modifications induced by the reduction treatment. Electrochemical impedance spectroscopy (EIS) and distribution of relaxation times (DRT) techniques were implemented to gain insights into the oxygen electrocatalysis occurring at the catalyst surface with and without the reduction treatment. Finally, e*x-situ* soft X-ray absorption spectroscopy (XAS) in total electron yield (TEY) was performed on the samples before and after the electrochemical measurements, to evaluate how the OER/ORR activity of the material can be triggered by structural modifications induced by the reduction treatment.

2. Results and discussion

2.1. As-synthesized properties of as-prepared and reduced LSFPt

Fig. 1a presents the X-ray powder diffraction (XRPD) patterns of the as-prepared and reduced LSFPt samples. The as-prepared LSFPt displays the characteristic (JCPDS 82-1961) pattern of $La_{0.6}Sr_{0.4}FeO_{3-\delta}$ (LSF), corresponding to a rhombohedral structure and R-3c space group. The absence of additional phases confirms the successful synthesis of the perovskite material. The reduction treatment at 500 °C does not alter the perovskite structure, as no secondary phases are detected in the pattern. From Fig. 1b, a shift toward lower angles is revealed. This shift can be related to lattice expansion and is the first indication of the successful reduction treatment. Previous studies have reported that high-temperature reduction treatments induce oxygen release in the LSF-

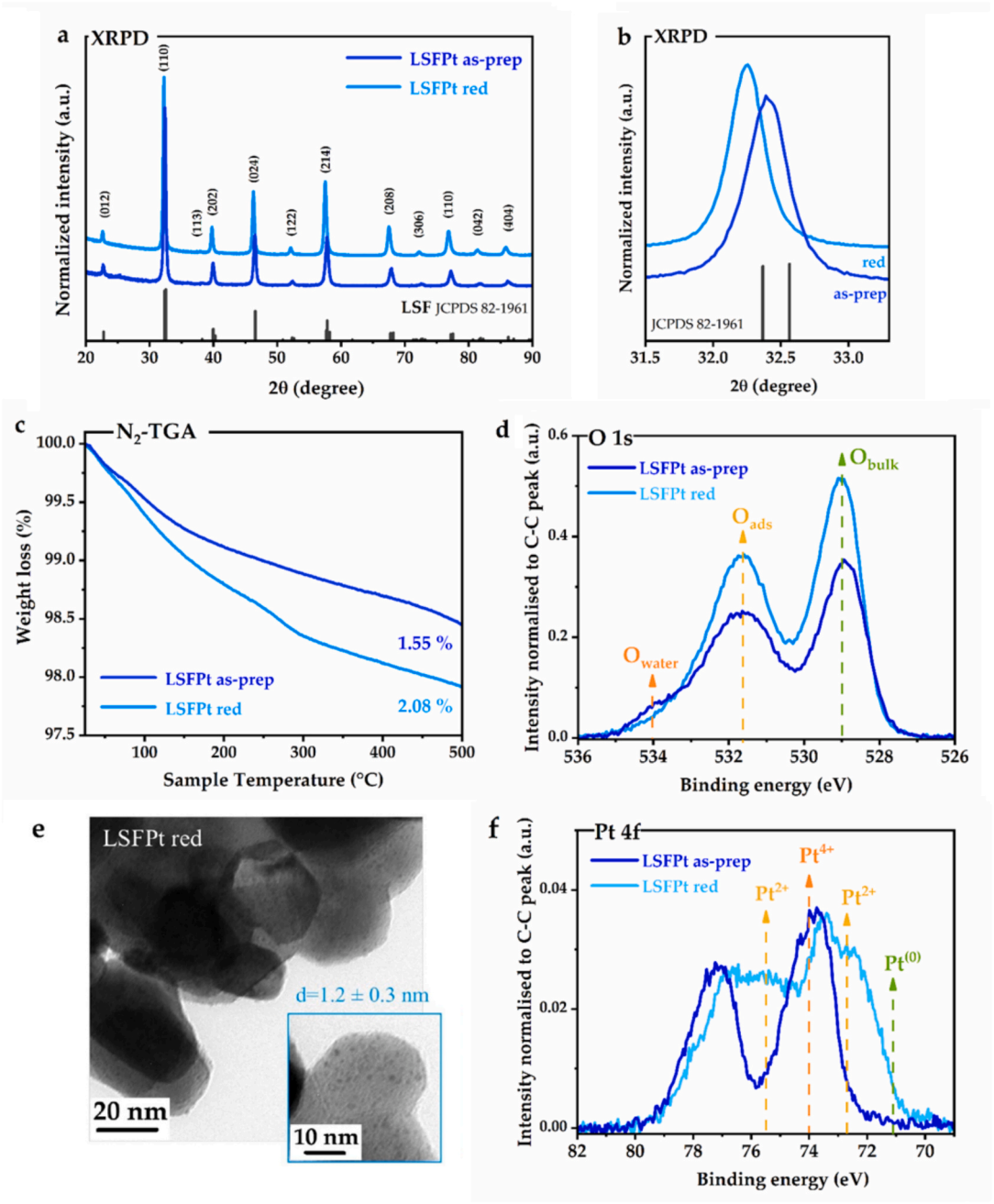

Fig. 1. As-synthesized properties of as-prepared and reduced LSFPt. a) XRPD with LSF pattern (JCPDS 82–1961) as reference. b) Enlargement of the most intense XRPD peak revealing the shift toward lower angles in the reduced LSFPt. c) TG analysis in N_2 atmosphere between 50 °C – 500 °C with a heating ramp of 5 °C·min^{-1}. d) O 1 s XPS spectra of as-prepared and reduced LSFPt. e) TEM micrograph of LSFPt after reduction treatment at 500 °C under flowing 5% H_2/Ar for 10 h. f) Pt 4f XPS spectra of as-prepared and reduced LSFPt.

based compounds, leading to the formation of oxygen vacancies and the reduction of B-site metal nanoparticles onto the surface [25,39,40]. In our case, Pt is expected to exsolve from the bulk and aggregate into nanoparticles on the material surface [23,34]. To evaluate the contribution of B-site exsolution to the structure, a size-strain plot analysis of XRPD spectra was performed and is presented in **Fig. S1**. The strain, an indicator of the stress level in the structure, is lower than that of the as-prepared LSFPt, measuring 1.7 × 10^{-2}% compared to 2.1 × 10^{-2}%. The reduced LSFPt material achieved the same strain value as the undoped LSF, used as a reference material (**Fig. S1**). The substitution of Fe^{3+}/Fe^{4+} ions with larger Pt^{4+}/Pt^{2+} ions at the B-site has shown an increase in lattice distortion, as previously reported [34]. Thus, the reduction in bulk strain of LSFPt after treatment in reducing conditions is likely due to the depletion of Pt^{4+}/Pt^{2+} ions in the lattice, resulting from the exsolution of Pt from the bulk to the surface of the perovskite, with the consequent relaxation of the lattice stress. The surface area of LSFPt before and after the reduction treatment was also assessed by BET method on the adsorption branch of the N_2 adsorption/desorption isotherms (**Fig. S2**). The reduced LSFPt sample presents a slightly higher surface area compared to the as-prepared one (18.00 ± 0.08 m^2/g and 15.83 ± 0.05 m^2/g, respectively), confirming the effective surface changes of the perovskite induced by the reduction treatment.

Thermogravimetric (TG) analysis in N_2 from 50 °C to 500 °C was used to get insights into the defect formation. Fig. 1c displays similar profiles for both samples; at temperatures below 150 °C, the weight loss is ascribable to the water desorption, and at higher temperatures to the

oxygen desorption from the surface. At 500 °C, the final weight loss is –1.55% for the as-prepared and –2.08% for the reduced sample, indicating an oxygen deficiency after the reduction treatment [34]. This is further confirmed by the comparison of TGA analysis carried out in air for both materials (see **Fig. S3** for details). X-ray photoelectron spectroscopy (XPS) measurements of the O 1 s region, presented in Fig. 1d, reveal differences in oxygen content between the two samples. The as-prepared LSFPt sample exhibits three distinct features: the O_{bulk} signal at 529.0 eV, corresponding to structural oxygen in the perovskite; the O_{ads} signal at 531.6 eV, associated with adsorbed species on the surface; and the O_{water} signal at 533.7 eV, attributed to adsorbed water [19,41]. For the reduced LSFPt sample, thermal treatment at 500 °C for 10 h significantly decreases the surface presence of adsorbed water, effectively eliminating the O_{water} contribution. With the reduction treatment, while the O_{ads} peak remains unchanged, the O_{bulk} peak shifts slightly by +0.2 eV toward higher binding energy. This shift suggests an increased presence of highly oxidative species (O_2^{2-}/O^-), likely due to the formation of oxygen vacancies within the structure, consistent with literature on oxygen vacancy formation [42–44]. The reduction treatment led to the exsolution of nanoparticles from the surface, as shown in the transmission electron microscope (TEM) micrograph in Fig. 1e and scanning electron microscope (SEM) micrograph in **Fig. S4a**. The LSFPt sample reduced at 500 °C exhibits a uniform distribution of Pt nanoparticles on the perovskite surface with an average diameter of 1.2 nm (particle size distribution in **Fig. S4b**). Undoped LSF sample after the same reduction treatment (10 h at 500 °C), showed the start of the surface nucleation step, with the presence of large and isolated Fe nanoparticles (scanning electron microscope, SEM, image **Fig. S4c**) and no other smaller nanoparticles features. This contrasts with the numerous and uniformly distributed nanoparticles observed on the reduced LSFPt perovskite (Fig. 1e). The hydrogen temperature programmed reduction (H_2-TPR) plot of the as-prepared LSF and LSFPt (**Fig. S4d**) demonstrates the high reducibility of Pt which shifts the surface reduction peak to lower temperatures. This shift indicates that Pt exsolution occurs at lower temperatures than Fe in the undoped LSF sample. The Pt 4f XPS spectra of as-prepared and reduced samples are reported in Fig. 1f. The as-prepared LSFPt exhibits two well-resolved peaks corresponding to $4f_{7/2}$ (around 74 eV) and $4f_{5/2}$ (around 77 eV) core levels, indicating the presence of Pt in multiple oxidation states, with Pt^{4+} being the dominant species [34,45]. In the reduced sample, new peaks appear at 72.5 eV and 75.5 eV, which are assigned to the reduced oxidation state of Pt^{2+} [46–50]. While metallic Pt^0 is not clearly identified due to the superposition of peaks from Pt^{2+} at 72.5 eV and Pt^0 at 71 eV, the data demonstrate that these highly dispersed Pt^{2+} species are the dominant state. The emergence of these reduced Pt signals, alongside the morphological changes observed in TEM/SEM (Fig. 1e, **Fig. S4a**), confirms the successful exsolution of Pt species triggered by the thermal reduction at 500 °C. The reduction treatment does not significantly affect the A-site cations (La and Sr) or the Fe valence state, as shown in the XPS spectra in **Fig. S5**. These results confirm the successful reduction treatment of the perovskite catalyst, with the presence of both oxygen defects and nanoparticles of reduced Pt species on the catalyst surface, key features for enhanced catalytic functionality. Given the presence of reduced Pt species on the surface, it is reasonable to expect that the ORR activity of the reduced sample will be lower than that of a metallic Pt benchmark catalyst. However, the nanoscale size and homogeneous distribution of the exsolved Pt particles are promising indicators. To evaluate this effect, the OER and ORR performance of the as-synthesized and reduced LSFPt samples were investigated in alkaline media.

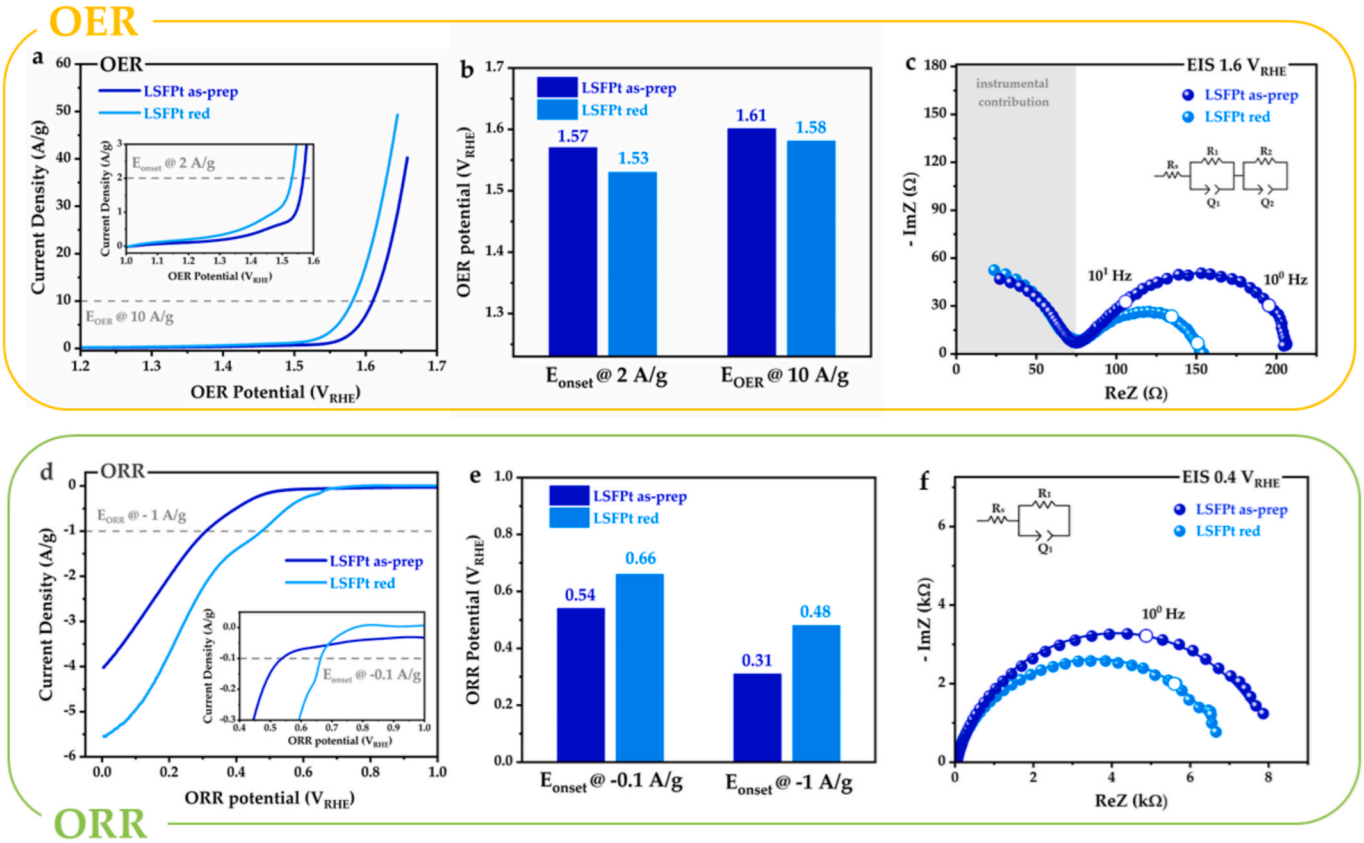

Fig. 2. Oxygen electrocatalysis performance of the as-prepared and reduced LSFPt. a) OER polarization curves recorded at 10 mV s^{-1} in air-saturated 0.1 mol L^{-1} KOH. b) OER potentials at the current density of 10 A g^{-1} and 2 A g^{-1} extracted from Fig. 2a. c) Nyquist plots collected at 1.6 V_{RHE} with the corresponding equivalent circuit fit. d) ORR polarization curves recorded at 5 mV s^{-1} in air-saturated 0.1 mol L^{-1} KOH. e) ORR potentials at the current density of –0.1 A g^{-1} and –1 A g^{-1} extracted from Fig. 2d. f) Nyquist plots collected at 0.4 V_{RHE} with the corresponding equivalent circuit fit.

2.2. Oxygen electrocatalysis

The OER and ORR catalytic activity in synthetic air-saturated 0.1 mol L^{-1} KOH was measured for the as-prepared and reduced LSFPt samples, and the results are presented in Fig. 2. The electrolyte choice was based on maintaining the same electrochemical environment for both oxygen reactions. To evaluate the OER catalytic activity, a series of 25 cyclic voltammetry (CV) cycles was carried out (**Fig. S6a**). The data presented are representative of different OER measurements carried out on at least three independent depositions using three different catalyst inks. The corresponding statistics can be found in **Fig. S7a-b**. The comparison between the last anodic scan of the two samples is presented in Fig. 2a. The reduced LSFPt material reaches a current density of 17.4 A g^{-1} at 1.6 V_{RHE}, 2.5-fold higher than that of the as-prepared LSFPt (6.9 A g^{-1}). As presented in the histogram in Fig. 2b, the reduced sample presents an onset potential (E_{onset}, potential to achieve 2 A g^{-1}) of 1.53 V_{RHE}, lower than 1.57 V_{RHE} of the as-prepared catalyst. Similarly, the OER potential (E_{OER}, potential to reach 10 A g^{-1}) is lower for the reduced LSFPt with respect to the as-prepared LSFPt (1.58 V_{RHE} and 1.61 V_{RHE}, respectively). These results demonstrate that the reduction treatment improves the OER performance of LSFPt, as evidenced by lower onset and OER potentials compared to the as-prepared catalyst. Electrochemical impedance spectroscopy (EIS) characterization was carried out at 1.6 V_{RHE} for both as-prepared and reduced samples (Fig. 2c). In general, the EIS spectra are fitted with two elements: one at high frequency related to non-faradaic processes at the catalyst surface, and the other at low frequency, directly related to the oxygen evolution reaction [51]. An $R_s(Q_1R_1)(Q_2R_2)$ circuit model was used to fit the Nyquist curves for both samples, and the fitting results are listed in **Table S1**. Looking at the Nyquist plot comparison in Fig. 2c, the polarization resistance of the reduced LSFPt decreased by 37% compared to the as-prepared sample. The higher activity from CV and lower polarization from Nyquist plot indicate that the reduced LSFPt catalyzes OER better than the as-prepared. This can be associated with the structural changes on the surface after the reduction treatment: the presence of surface oxygen defects is crucial for the OER activity of perovskite oxides [19,52,53]. In addition, the presence of exsolved nanoparticles containing reduced Pt species on the surface is also expected to influence the ORR, thus enhancing the catalyst's bifunctionality when compared to the as-synthesized LSFPt.

Carbon additives are commonly incorporated during ink preparation to enhance conductivity and, consequently, improve the ORR performance. However, to reliably assess the intrinsic activity toward ORR and OER, the same ink composition (without carbon additives) and the same electrolyte (air-saturated 0.1 mol L^{-1} KOH) were used for both protocol measurements. The ORR catalytic activity was assessed using the same electrolyte by a series of 5 CV cycles (**Fig. S6b**). The data presented are representative of different ORR measurements carried out on at least three independent depositions using three different catalyst inks. The related statistical data are provided in **Fig. S7c-d**. The 5th cathodic scans from both samples are presented in Fig. 2d. The activity of the reduced LSFPt sample is 2.8-fold higher than the as-prepared one, being –1.4 A g^{-1} and –0.5 A g^{-1} at 0.4 V_{RHE}, respectively. The histogram in Fig. 2e demonstrates that the reduction treatment leads to an improvement of the onset potential (E_{onset}, potential to reach –0.1 A g^{-1}) from 0.54 V_{RHE} for the as-prepared to 0.66 V_{RHE} for the reduced LSFPt. The ORR potential (E_{ORR}, potential to reach –1 A g^{-1}) is also improved from 0.31 V_{RHE} for the as-prepared to 0.48 V_{RHE} for the reduced LSFPt. These improvements highlight the positive effect of the reduction treatment on the catalyst's ORR performance. EIS characterization was performed at 0.4 V_{RHE}, and the resulting Nyquist plots for both catalysts are presented in Fig. 2f. Usually, ORR EIS curves are fitted with two elements, one associated with the charge transfer process of O_2 reduction, and one related to the adsorption of oxygen intermediates [54]. However, the ORR resistance on both samples is of the order of kΩ, so the second element can be neglected, and Nyquist curves were fitted with only one element using a $R_s(Q_1R_1)$ circuit model (**Table S2**). This relatively high resistance for the reduced sample may be partially attributed to the presence of Pt^{2+} species, as revealed by XPS (Fig. 1f), which are generally less active than metallic Pt for ORR. This observation corroborates with the relatively lower ORR activity compared to metallic Pt-based catalysts. Nevertheless, the reduced treatment improves the ORR activity, reducing the polarization resistance by 17% compared to the as-prepared LSFPt. The increased ORR activity of the perovskite sample after the reduction treatment can be attributed to the presence of nanoparticles containing reduced Pt species exsolved on the perovskite surface, which provide additional active sites for the reaction. To qualitatively evaluate the stability of the exsolved nanoparticles after OER and ORR measurements, *post-mortem* SEM analysis was carried out and presented in **Fig. S8**. Although the identification of such small nanoparticles is hampered by the presence of residual Nafion and KOH, the characteristic surface roughness attributed to the exsolved phase remains evident for both as-deposited ink (**Fig. S8a**) and for the samples retrieved after the 25 OER cycles and after the 5 ORR cycles (**Fig. S8b-c**). The observation that the surface morphology remains intact after cycling suggests that the socketed nanoparticles are structurally stable, highlighting the potential of this exsolution approach for durable bifunctional catalysis.

The influence of reduction temperature (500 °C vs. 750 °C) on ORR activity for LSFPt is summarized in **Table S3**. The LSFPt reduced at 500 °C exhibits superior ORR performance compared to the LSFPt reduced at 750 °C. Notably, while the higher temperature promotes the formation of larger and well-defined Pt nanoparticles on the surface [34], the resulting activity declines toward levels observed in the as-prepared material. This indicates that the lattice disruption occurring at 750 °C is detrimental for the overall catalytic process, outweighing the benefits of larger metallic surface sites. In contrast, the 500 °C treatment achieves an ideal balance, successfully exsolving Pt nanoparticles while preserving the structural integrity of the perovskite host, thereby yielding optimized performance. More information in **Fig. S9 a-b** of the Supporting Information. An evaluation of the role of exsolved Pt nanoparticles is provided in **Table S3**, which compares the ORR metrics of undoped LSF and Pt-doped LSFPt after identical reduction treatments at 500 °C. In summary, the enhanced ORR activity is driven by the strong electronic interaction between the exsolved nanoparticles containing reduced Pt species and the oxide matrix, the synergy with oxygen vacancies, and the preservation of the perovskite host, which outweighs the benefits of larger metallic surface sites. The results demonstrate that while reduction-induced oxygen vacancies contribute to activity, they are insufficient on their own; the presence of surface-exsolved Pt nanoparticles is essential for achieving significantly enhanced electrocatalytic performance. The SEM images of the two reduced catalysts are presented in **Fig. S4**, and more information is in **Fig. S9 c-d** of the Supporting Information. This result highlights exsolution as an effective strategy for developing catalysts with a unique surface composed of distinct and complementary active sites for both OER and ORR. Another descriptor that is commonly used to evaluate the electrocatalysts' bifunctionality is the potential difference in the same environment between the OER and ORR, $\Delta E = E_{OER} - E_{ORR}$ [14]. The ΔE obtained for the LSFPt sample after the reduction treatment is 1.05 V, which is 0.23 V lower than that of the as-prepared sample (ΔE = 1.28 V). Overall, while the absolute metrics of the reduced LSFPt do not reach the benchmarks of the state-of-the-art Pt/C for ORR and $NiFeO_x$ for OER in alkaline conditions, the system offers distinct structural advantages. To contextualize these results, the reduced LSFPt was compared with a 20 wt% Pt/C benchmark measured under the same testing conditions. While Pt/C typically exhibits a higher ORR onset potential (1.0 V_{RHE} vs. 0.81 V_{RHE} for LSFPt, **Fig. S9e** and **Table S3**), it remains susceptible to oxidative carbon corrosion during bifunctional testing. In contrast, the LSFPt system utilizes the perovskite lattice as both a stable support and an active co-catalyst. This creates a unique, metal-socketed interface that circumvents the degradation issues inherent to carbon-supported

benchmarks while leveraging metal-support synergy. Ultimately, the 2.5-fold increase in mass activity observed upon exsolution in LSFPt demonstrates the effectiveness of this approach as a tool for activating the perovskite surface for bifunctional oxygen catalysis.

2.3. DRT evaluation for OER/ORR overpotential contributions

To gain further insight into the different processes occurring at the catalysts during oxygen electrocatalysis, distribution of relaxation times (DRT) deconvolution on EIS data was performed for the as-prepared and reduced LSFPt perovskites. The DRT analysis is a deconvolution method that allows for switching from a Z_{Im} *vs.* Z_{Re} Nyquist plot to a "γ function" *vs.* "frequency DRT" plot [55]. In this way, no prior knowledge of the system is needed, and the analysis provides a distribution function in which single impedance contributions can be observed [56]. From DRT plots, different information can be extracted: the peak position determines the frequency at which the single mechanism step occurs, while the total area under the peak is proportional to the polarization resistance related to that overpotential contribution. The total polarization resistance can be calculated as the sum of the resistances associated with the different peaks [55–57]. DRT applications to RDE studies are still relatively rare; most works focus on the analysis of complete cells. In general, in the study of different electrochemical devices, three main overpotential contributions are detectable with the use of DRT analysis: mass transport (10^{-1}–10^{1} Hz), charge transport of the electrochemical reaction (10^{0}–10^{3} Hz) and ion transport phenomena ($> 10^{3}$ Hz) [58–61]. However, if a simpler three-electrode cell system is considered, similar considerations can be made [62,63]. Although a one-to-one peak attribution is challenging, a DRT evaluation can be done by examining the system at different stages of oxygen reactions. The scope of this section is to qualitatively assign peaks at different frequencies to different processes, in order to understand which processes can be favored by the reduction treatment.

DRT analysis at various OER potentials was conducted on the LSFPt reduced sample to assess the evolution of peak positions and their resistances under different applied potentials, aiding in their attribution to different overpotential contributions. The Nyquist plots are displayed in **Fig. S10a**, while the resulting DRT spectra and histograms with peak resistances are presented in Fig. 3a and 3b.

Considering the DRT plot in Fig. 3a, each curve can be divided into two regions based on the potential dependence of the peaks. The higher frequency peaks with low-dependency from the potential (P_1 and P_2) can be referred to the ionic (OH^-) transport in the porous structure of the catalyst layer [63–65]. On the other hand, the lower frequency peaks (P_3, P_4, and P_5) are highly related to the potential changes: P_3 peak decreases and merges with the other medium frequencies contributions by increasing the applied potential, from 1.58 V_{RHE} on, while P_4 decreases, shifting its characteristic frequency to higher values. These lower-frequencies processes can be associated with the OER reaction as a combination of charge transfer and production rate of intermediates [63,64,66]. Moreover, as shown in the histogram of Fig. 3b, the decrease of P_4 resistance follows an almost exponential-like trend with increasing potential. This behavior is typically attributed to the accelerated charge transfer process of adsorbate oxygen species induced at high potentials during OER reaction [65,67]. An additional low frequency P_5 contribution becomes visible up to 1.58 V_{RHE}, likely do to the diffusion of produced oxygen species into the perovskite film [58,68]. To study the differences in OER regimes between as-prepared and reduced LSFPt, the

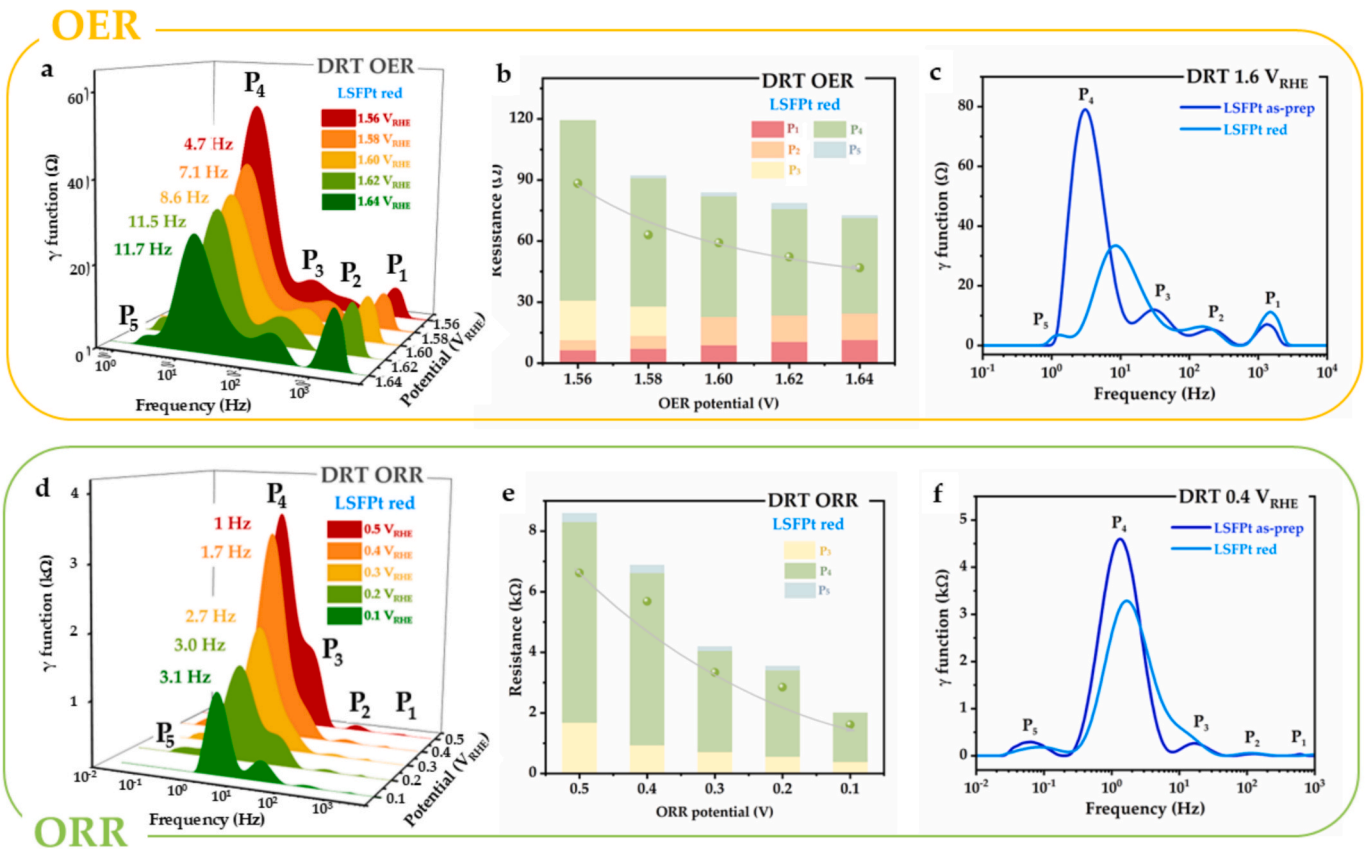

Fig. 3. OER/ORR DRT analysis of LSFPt samples. a) DRT spectra at different OER potentials and b) the related histogram of peak resistances of the reduced LSFPt. The green circles at each potential represent the resistance values extrapolated for the P_4 process, which follow an exponential-like trend with potentials. c) Comparison of DRT spectra at 1.6 V_{RHE} for as-prepared and reduced LSFPt samples. d) DRT spectra at different ORR potentials and e) the related histogram of peak resistances of the reduced LSFPt. The green circles at each potential represent the resistance values extrapolated for the P_4 process, which follow an exponential-like trend with potentials f) Comparison of the DRT spectra at 0.4 V_{RH} for as-prepared and reduced LSFPt samples.

DRT on Nyquist plot collected at 1.6 V_{RHE} has been compared and is presented in Fig. 3c. The high frequency peaks P_1 and P_2 remain largely unchanged between the two samples, suggesting that the reduction treatment does not affect ion transport during the electrochemical process. Whereas a more significant difference is observed in the 10^0-10^2 Hz frequency range, as better highlighted in **Fig. S10b** histogram. The most resistive OER-related P_4 peak exhibits a 67% lower resistance for the reduced sample compared to the as-prepared one, with a shift to higher frequencies, from 3.05 Hz to 8.56 Hz. This evidence, along with the small gas diffusion P_5 peak around 1 Hz present only for the reduced sample, indicates a faster and less resistive OER process compared to the as-prepared one, in agreement with previously reported OER activity.

As in the OER case, a DRT analysis was performed for the reduced LSFPt within the ORR potential range. The resulting DRT plot is presented in Fig. 3d, with the corresponding Nyquist plots shown in **Fig. S10c**. Despite the lower intensity, the high frequency peaks P_1 and P_2 appear less affected by changes in applied potential, confirming their association with ionic transport. In contrast, P_3, P_4 and P_5 peaks are strongly dependent on the changes in the potential, with their intensity decreasing as the ORR process improves, as shown in the histogram in

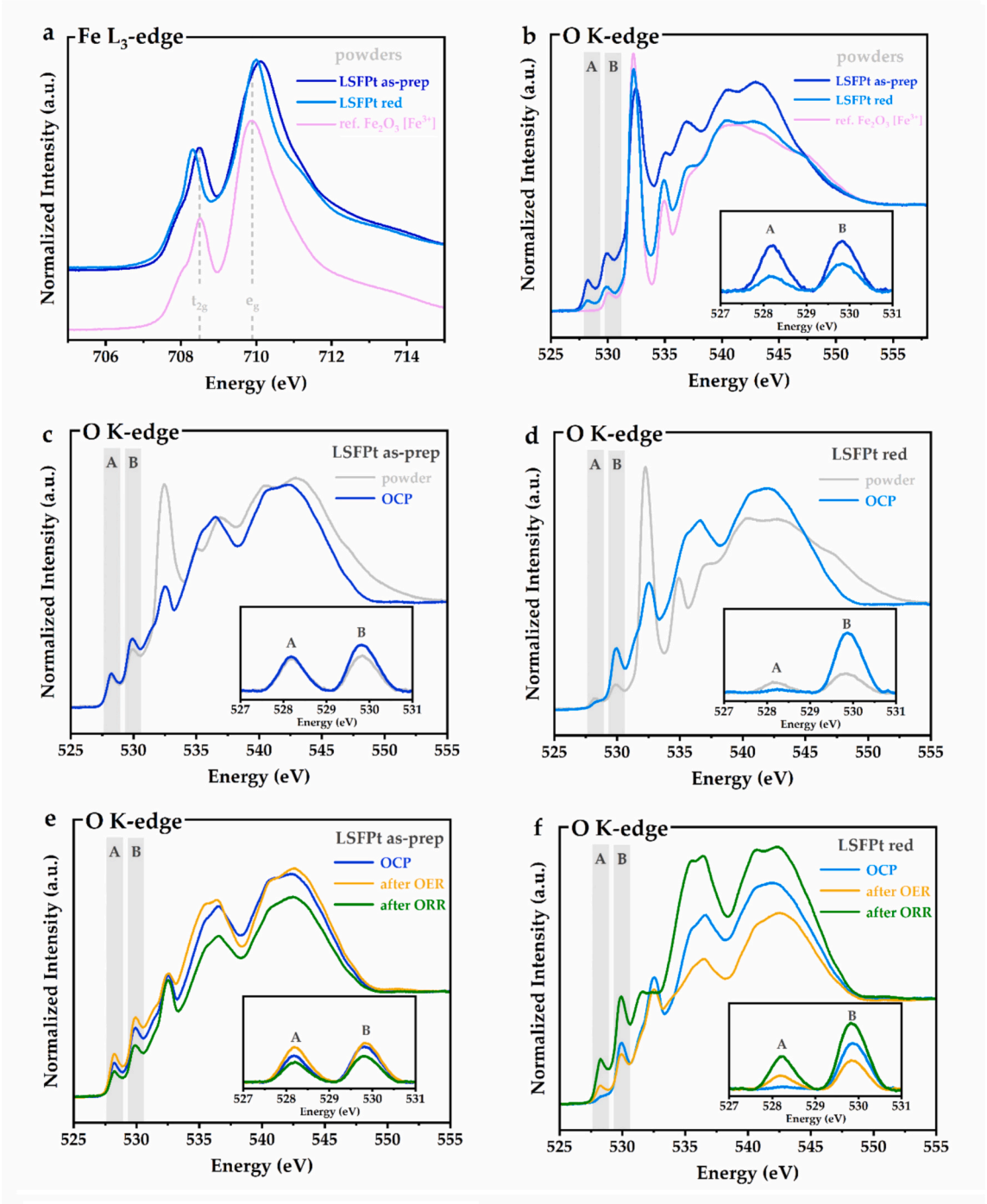

Fig. 4. Surface sensitive *post-mortem* soft XAS characterization. a) Fe L_3-edge and b) O K-edge XAS spectra of as-prepared and reduced LSFPt powders, along with Fe_2O_3 reference (Fe^{3+}). Comparison of the O K-edge spectra of the bare powder and the OCP sample of c) the as-prepared LSFPt and d) the reduced LSFPt samples. Comparison of the O K-edge spectra before and after OER or ORR for e) the as-prepared LSFPt and f) the reduced LSFPt samples. The data in the insets are presented after linear background subtraction in the 527–531 eV region.

Fig. 3e. P_3 and P_4 can be attributed to ORR charge transfer reaction occurring at the catalyst surface, given their net improvement in both resistance and kinetics of such process toward lower potential, while the lower frequency P5 is likely related to the O_2 gas diffusion into the perovskite film [58,62,69,70]. To evaluate the ORR process for both samples, the DRT plots on Nyquist plots collected at 0.4 V_{RHE} are compared in Fig. 3f. In this case, the ion transport peaks at high frequencies (P_1 and P_2) cannot be distinguished due to the higher resistance of the charge transfer process peaks. For both samples, the ORR-related P_4 peak around 10^0 Hz is identified as a rate-determining step (**Fig. S10d**). The reduced LSFPt displays a 25% reduction in the P_4 process resistance, along with a shift toward higher frequencies compared to the as-prepared one, highlighting the enhanced activity of the catalyst surface towards ORR after the reduction treatment. In conclusion, both the OER and ORR DRT analyses confirm that the surface reduction treatment is a successful strategy to improve the kinetics of oxygen reactions on the perovskite surface without affecting other overpotential contributions during oxygen electrocatalysis.

2.4. Evaluation of surface by soft XAS of the pristine powders and post-mortem samples

To illustrate the surface evolution of the as-prepared and reduced LSFPt catalysts following OER and ORR, ex-situ soft X-ray absorption spectroscopy (sXAS) in total electron yield (TEY) mode was performed on the pristine powders as well as before and after electrochemical measurements (Fig. 4). Commercial reference material Fe_2O_3 has been used as the standard for Fe^{3+} oxidation state. As a first step, soft XAS analysis was carried out on pristine samples (powder form, before any electrochemistry testing) to assess surface changes induced by the reduction treatment on LSFPt. The complete Fe L-edge spectra in **Fig. S11** exhibit similar spectral shapes for both samples, with two L_3 and L_2 edges, which further split into t_{2g} and e_g bands [20]. Focusing on Fe L_3-edge spectra in Fig. 4a, the as-prepared sample exhibits a main band at 709.9 eV, slightly shifted to higher absorption energies (+0.23 eV) compared to the Fe^{3+} reference, along with a broadening of the high-energy shoulder. This shift and broadening of the band suggest the presence of Fe in a higher oxidation state (Fe^{4+}), which is consistent with this type of Sr-doped ferrite perovskites [20,71,72]. In contrast, the reduced sample displays a smaller shift relative to the Fe^{3+} reference (+0.11 eV), indicating that the Fe oxidation state at the surface is slightly lower on the reduced LSFPt sample because of the reduction treatment. Importantly, the perovskite structure remains intact after the reduction treatment, as confirmed by XRPD in Fig. 1a [31,32,71]. No significant changes of Fe L-edge were observed before and after electrochemistry. More information about Fe L-edge spectra can be found in Supplementary Information (**Fig. S12**).

The full O K-edge spectra collected for the LSFPt samples are shown in Fig. 4b. With respect to Fe L-edge, O K-edge spectrum has a more complex shape, and the band attribution is more challenging. The features at higher energies (>534 eV) can be related to La*4d* / O*2p* and B-site *4sp*/ O*2p* electronic states, while the most characteristic region between 526–534 eV depends on the dipole transition from O*1s* core level to O*2p* states hybridized with B-site metal *3d* states [73–75]. The O K-edge spectra of LSFPt samples are similar to other LSF-based oxide spectra observed by other authors [76,77]. Two main bands can be found at low energy: an edge band around 530 eV and a pre-edge band around 528 eV, related to $t_{2g}\downarrow$ unoccupied state and $e_g\uparrow$ partially unoccupied state, respectively. Usually, in the perovskite systems the intensity of these peaks is proportional to the number of *d* electrons in the orbital and then to the oxidation state of the metal in the B-site [73]. Unlike both LSFPt samples, the Fe^{3+} reference does not exhibit the pre-edge at 528 eV. This feature is related to the hole-states induced by the Sr-doping in this type of ferrite oxides: the presence of Sr cations at the A-site induces the oxidation of Fe from Fe^{3+} ($t_{2g}3\ e_g2$) to Fe^{4+} ($t_{2g}3\ e_g1$), changing the electronic configuration [20,78,79]. Focusing on the $t_{2g}\downarrow$ (labeled B in Fig. 4b) and $e_g\uparrow$ (labeled A in Fig. 4b) bands, the intensity of both A and B bands decreases after reduction treatment. Moreover, A/B area ratio decreases from 0.86 in the as-prepared LSFPt to 0.43 in the reduced sample (see Fig. 4b). This reduction in intensity and the lower A/B ratio suggest an increased electron density in the B-site $e_g\uparrow$ orbital, which can suggest a partial reduction of the metals in the B-site [31,80,81], in our case would be Fe and Pt. This effect is likely related to the increased oxygen defects, which have been shown to be beneficial for the OER/ORR performance.

To get qualitative information about the evolution of the surface after electrochemistry measurements, O K-edge was collected before and after OER/ORR electrochemical routines. At first, the interaction of the samples with the electrolyte was assessed by collecting the O K-edge spectra of the drop-casted sample after immersion in 0.1 mol L^{-1} of KOH electrolyte for 15 min under open circuit potential conditions (labeled as OCP). Fig. 4c,d present the comparison between powder and open circuit potential (OCP) spectra for as-prepared and reduced LSFPt, respectively. In both cases, the interaction with the electrolyte changes the shape of the signal, especially in the high-energy range (>534 eV), due to the perovskite interaction with H_2O/OH^- and Nafion solution [82]. Focusing on the low-energy range (<534 eV), the as-prepared and the reduced LSFPt have opposite behavior. For the as-prepared, the OCP spectrum displays similar intensities for both A and B features at around 528 and 539 eV, respectively (Fig. 4c), indicating minimal changes in the perovskite surface. In contrast, the reduced LSFPt presents significant changes in both bands (Fig. 4d), suggesting a stronger interaction between the defective surface and OH^- species from the electrolyte. A similar trend has been reported for CoO_x/CeO_2 and CoO_x catalysts, where increased in oxygen deficiency of the doped CoO_x/CeO_2 led to more pronounced modifications in the O K-edge and superior catalytic performance compared to undoped CoO_x [83].

The O K-edge spectra of both LSFPt samples after OER and after ORR measurements were also evaluated (Fig. 4e,f). The evolution of the low-energy features A and B, along with the A/B area ratios, is compared for both samples in **Fig. S13**. For the as-prepared sample (Fig. 4e), the intensity and the shape of the O K-edge bands remain largely unchanged with respect to the OCP spectrum. As shown in **Fig. S13**, the values of the A and B peak areas and the A/B area ratio remain stable after the oxygen reduction and evolution reactions, as indicated by the almost horizontal lines. This suggests that the oxygen environment on the surface in the as-prepared sample is mostly preserved after electrochemical measurements. Additionally, both features show consistent trend after OER and after ORR electrochemical routines, as highlighted in the enlargement of Fig. 4e. In contrast, the reduced LSFPt exhibits more evident spectral changes after oxygen reactions compared to the OCP spectrum (Fig. 4f). After OER, the A feature increases in intensity, while the B feature decreases, resulting in an overall increase in A/B area ratio (**Fig. S13**). After ORR, both A and B features exhibit a pronounced increase in intensity compared to the OCP spectrum. Moreover, a distinct spectral feature appears at 531 eV (Fig. 4f). These spectral changes suggest that the reduced sample experienced more surface modifications than the as-synthesized one, possibly involving changes in oxygen coordination and surface adsorption. As suggested by Mueller *et. al.* [74] when evaluating the role of A and B features in a similar type of perovskite under *operando* conditions, the increase in intensity of pre-edge feature A could be an indication of the annihilation of the oxygen vacancies due to the presence of oxygen adsorbates on the catalyst surface, while the change in intensity of feature B is more likely related to changes in covalent bonding between B-site metal and oxygen on the surface [74]. Although our spectra were collected *ex situ*, the observed changes in the reduced sample may suggest analogous surface modifications, especially considering the presence of oxygen deficiency and reduced Pt species on the surface.

3. Conclusion

In this work, we successfully exsolved nanoparticles containing reduced Pt species from $La_{0.6}Sr_{0.4}FeO_{3-\delta}$ doped with 5 mol% Pt and demonstrated that this *in-situ* exsolution significantly enhances the oxygen electrocatalytic performance of a ferrite perovskite in alkaline media. The mild-temperature (500 °C) reduction treatment promotes the exsolution of reduced Pt-containing nanoparticles onto the perovskite surface, while generating surface oxygen defects without compromising the structural integrity of the perovskite material. This dual effect enhances both OER and ORR activity. Structural and morphological characterizations reveal a defect-rich surface decorated with well-dispersed Pt-containing exsolved nanoparticles approximately 1.2 nm in size. In the electrochemical evaluations, the reduced LSFPt exhibits more than 2.5-fold higher activity compared to the as-prepared sample for both the OER and ORR, with a reduction in polarization resistance of 37% and 17%, respectively. EIS and DRT deconvolution analyses further confirm the positive effect of the reduction treatment, revealing decreased resistance in the medium-frequency range associated with charge transfer processes for both reactions. Additionally, a qualitative surface sensitive *ex-situ* XAS analysis at O K-edge suggests more surface alterations in the reduced sample than the as-synthesized one, likely involving changes in oxygen coordination and adsorption. While the reduced LSFPt catalyst's performance does not meet the benchmark of the state-of-the-art materials Pt/C for ORR and NiFeOx for OER, it still shows significant enhancement compared to the untreated sample. This one-step reduction strategy, which simultaneously introduces defects and exsolves ORR-active nanoparticles containing reduced Pt species on the catalyst's surface, provides a valuable methodological insight for the community to harness oxygen electrocatalysis across a range of perovskite and related OER-active materials.

4. Experimental sections

4.1. Materials synthesis

The synthesis of $La_{0.6}Sr_{0.4}Fe_{0.95}Pt_{0.05}O_{3-\delta}$ (LSFPt) was carried out via citrate–nitrate solution combustion method, following a procedure described in detail elsewhere [34]. In brief, nitrate precursors La $(NO_3)_3{\cdot}6H_2O$ (Alfa Aesar©, 99.999%), $Sr(NO_3)_2$ (Aldrich®, 99.995%), $Fe(NO_3)_3{\cdot}9H_2O$ (Aldrich®, 99.99+%) and $H_{12}N_6O_6Pt$ (Alfa Aesar©, 99.995%), were dissolved in distilled water with 1:1 ratio of citric acid monohydrate (Aldrich, 99.5%) as fuel and complexing agent. After the evaporation of water, the gel was ignited at 350 °C, and the obtained amorphous ashes were calcined at 750 °C, 5 °C·min^{-1} for 6 h to obtain the final compound. The temperature-controlled reduction treatment was performed by treating the LSFPt powder at 500 °C, 5 °C·min^{-1} under the flux of 5% H_2/Ar mixture for 10 h, at a flow rate of 100 cm^3•min^{-1}.

4.2. Structural and morphological characterizations

X-ray powder diffraction (XRPD) patterns were obtained using a Philips X-Pert Pro 500 diffractometer with Cu Kα radiation ($\lambda = 1.54056$ Å) from 20° to 90° in 2θ with 0.015° step size and 10 s time per step. The surface area was assessed by Brunauer-Emmett-Teller (BET) method with a TriStar II Plus Micromeritics apparatus. Samples were pretreated at 350 °C under nitrogen flow and the adsorption/desorption isotherms were acquired at −196 °C. The BET specific surface area was evaluated in the 0.05–0.3p/p_0 relative pressure range of the adsorption branch. Thermogravimetric (TG) analyses were carried out on 30 mg of sample loaded in a Pt crucible under N_2 flux using a TG-DSC 1 (Mettler Toledo, STAR system). The mass loss was recorded between 50 °C and 500 °C, with a heating ramp of 5 °C·min^{-1}. The buoyancy effect was subtracted. Hydrogen temperature programmed reduction (H_2-TPR) was performed with AutoChem 2950 HP Micromeritics automated flow through device with a TCD detector. The measurement was performed up to 1000 °C, flowing 5% H_2/Ar gas mixture at 30 cm^3•min^{-1} during the heating process, recording the H_2 consumption. CuO (99.99%, Aldrich®) was reduced for TCD calibration. The morphological analysis of both as-prepared and reduced LSFPt samples was performed using a 200 kV Transmission Electron Microscope (TEM ZEISS LIBRA200FE) and a Field Emission Scanning Electron Microscope (FE-SEM Leo SUPRA^{TM} 35 Carl Zeiss SMT).

The XPS spectra were acquired with a VG ESCALAB 220iXL spectrometer (Thermo Fisher Scientific) with a detection depth of 7–10 nm. The instrument was calibrated on a clean silver surface by measuring the Ag $3d_{5/2}$ peak at a binding energy (BE) of 368.25 eV with a full width at half-maximum (FWHM) of 0.78 eV at a pass energy of 30 eV. Focused monochromatized Al Kα radiation (1486.6 eV). The beam size was ~500 μm^2. The pressure in the analysis chamber was approximately 2•10^{-9} mbar. All survey spectra were recorded with a dwell time of 10 ms, using the pass energy of 70 eV in steps of 0.5 eV. The spectra acquired in a narrow energy scan were recorded using a pass energy of 20 eV in steps of 50 meV and a dwell time of 50 ms. The binding energy scale was calibrated using the Super-C carbon C1s peak (C–C binding energy of 284.8 eV). All intensities are normalized to the signal of C–C at 284.8 eV. Measurements were performed directly on the powder samples grounded in the agate mortar with 10 wt% of carbon black pearl (2000 carbon black, Cabot Corporation).

4.3. Electrochemical measurements

The electrochemical measurements were carried out in a three-electrodes electrochemical cell at room temperature, using a rotating disk electrode (RDE) to load the catalyst to act as the working electrode. The setup is composed of a potentiostat (Biologic, VMP-300) and a rotation speed-controlled motor (Pine Instrument Co., AFMSRCE). The reference electrode (RE) and counter electrode (CE) were a Hg/HgO electrode and a gold mesh, respectively. The electrolyte used was 0.1 mol L^{-1} KOH (pH 13) prepared by dissolving KOH pellets (99.99% Sigma Aldrich) in ultrapure water. Prior to the electrochemical measurement, to keep the same electrochemical environment for both oxygen reactions, the electrolyte was saturated by flowing synthetic air (20% O_2) for 30 min, and the flow was maintained throughout the experiments. The catalyst ink was prepared by adding 5 mg of catalyst in a mixed solution of 0.5 mL ultrapure water, 2 mL isopropyl alcohol (IPA), and 10 μL Nafion solution (Sigma Aldrich, 5% wt) as a binding agent, and sonicating for 30 min. Nafion was used as a dispersant and binding agent to ensure strong mechanical attachment of the film to the glassy carbon disk. Although Nafion is a proton-conducting ionomer, it is widely used in alkaline RDE studies due to its excellent mechanical and electrochemical stability. It is important to point out that while the negative charge functional groups in Nafion may locally interact with hydroxide ions from the electrolyte, these effects do not significantly alter the overall pH near the catalyst during the RDE experiment [84]. The electrode was prepared by drop casting 10 μL of catalyst ink on the surface of polished glassy carbon (GC, 0.196 cm^2) in the RDE, with a final catalyst mass loading of 0.02 mg. All specified potentials in this study were given concerning the reversible hydrogen electrode (RHE) scale indicated with the unit V_{RHE}. The potential difference was determined with the calibration of the used reference electrode against a polycrystalline platinum disc (0.196 cm^2, Pine Research Instrumentation, Durham, NC, USA) immersed in the hydrogen-saturated electrolyte. The electrochemical protocol for determining the OER activity for the synthesized catalysts included cyclic voltammetry (CV) between 1.0 V_{RHE} to 1.7 V_{RHE} (25 times) at a scan rate of 10 mV s^{-1} and rotation at 900 rpm. For the ORR protocol, CV between 0.0 V_{RHE} to 1.0 V_{RHE} (5 times) at a scan rate of 5 mV s^{-1} and rotation at 1600 rpm. The measured ORR current was corrected for capacitive contribution by performing the same ORR protocol in Ar-saturated electrolyte. To better evaluate the electrocatalytic versatility of the samples towards OER/ORR, the

same ink composition was used, avoiding the addition of carbon for ORR measurement. To overcome the GC influence, the same support was used with the same surface preparation before and after the measurements. The ORR activity of GC was measured before every drop cast. The potentials were corrected for ohmic drop using electrochemical impedance spectroscopy (EIS) analysis, and all measured currents were normalized by the mass of the catalyst. EIS was carried out from 1 MHz to 0.1 Hz frequency range with an alternating current (AC) signal amplitude of 5 mV. EIS spectra were acquired at fixed potentials of 1.6 V_{RHE} and 0.4 V_{RHE} for OER and ORR, respectively. For the reduced sample, the study of the evolution of EIS spectra at different potentials was implemented for both OER and ORR. For all the EIS measurements, the distribution of relaxation times (DRT) method was used for the deconvolution of the impedance contribution related to the different reaction processes. DRT analysis was carried out using a MATLAB tool developed by Ciucci *et al.* [55].

4.4. Statistical analysis of electrochemical measurements

The data presented in Fig. 2 are representative of multiple electrochemical measurements performed on at least three independent depositions from three different catalyst inks. Statistical analysis for both oxygen reactions is provided in **Fig. S7** in the Supplementary Information. The current profiles shown in **Fig. S7a-c** and the potential values at different current densities in **Fig. S7b-d** were calculated as the average of three independent measurements, with error bars indicating the standard deviations. Both OER and ORR results presented in Fig. 2 are consistent with these statistics and fall within the reported error margins.

4.5. Soft X-ray adsorption measurements

The *ex-situ* soft X-ray absorption spectroscopy (XAS) measurements were performed in the low-energy branch of the PHOENIX (X07MB) beamline at the Swiss Light Source (SLS) at the Paul Scherrer Institute (PSI), Switzerland. The spectra were recorded in continuous mode, recording the total-electron yield (TEY) every 0.025 eV, at room temperature in high vacuum (10^{-6} mbar). The scan rate was 80 eV per 3 min (26.67 eV min^{-1}). The detection depth for the TEY measurement is <10 nm. All spectra were divided by the I_0 signal of an Au grid positioned between the sample and the X-ray source. The measurements on as-prepared and reduced LSFPt samples, along with the commercial Fe_2O_3 used as a reference material, were carried out on the bare powders attached to a carbon tape and mounted on a copper holder. The same measurements were carried out on the materials before and after electrochemistry, on a glassy carbon support. The spectra before electrochemistry were acquired after immersing the working electrode in 0.1 mol L^{-1} KOH electrolyte and collecting the open circuit potential (OCP) for 15 min, samples labeled as "OCP". The spectra after electrochemistry were measured on the samples that underwent the entire OER/ORR electrochemical routine outlined previously, samples labeled as "after OER" and "after ORR". The O K-edge and Fe L-edge spectra were normalized using distinct methods using ATHENA and Origin, which were verified to yield consistent results. For Fe L-edge spectra, normalization was performed by first calculating a total background from the signal below the edge and subtracting this value for the whole spectra, followed by normalizing the entire spectrum to the intensity of the most prominent peak. For O K-edge spectra, normalization was performed by fitting and subtracting a pre-edge polynomial and then normalizing the post-edge by a representative intensity region. Example spectra illustrating each normalization are provided in the Supporting Information (**Fig. S14**). To quantify the O K-edge peak areas, a linear background was fitted and removed between the two adjacent local minima, and the area under the signal was integrated, as described by Suntivich *et al.* [73].

CRediT authorship contribution statement

Anna Paola Panunzi: Writing – review & editing, Writing – original draft, Visualization, Validation, Methodology, Investigation, Formal analysis, Data curation, Conceptualization. **Leonardo Duranti:** Writing – review & editing, Investigation, Formal analysis. **Elisabetta Di Bartolomeo:** Writing – review & editing, Visualization, Validation, Supervision, Project administration, Methodology, Investigation, Funding acquisition, Formal analysis, Data curation, Conceptualization. **Jinzhen Huang:** Writing – review & editing, Investigation, Formal analysis. **Camelia N. Borca:** Writing – review & editing, Investigation, Formal analysis. **Thomas Huthwelker:** Writing – review & editing, Investigation, Formal analysis. **Dominika Baster:** Writing – review & editing, Investigation, Formal analysis. **Mario El Kazzi:** Writing – review & editing, Investigation, Formal analysis. **Marcello Marelli:** Writing – review & editing, Investigation, Formal analysis. **Emiliana Fabbri:** Writing – review & editing, Visualization, Validation, Methodology, Investigation, Funding acquisition, Formal analysis. **Juliana Bruneli Falqueto:** Writing – review & editing, Writing – original draft, Visualization, Validation, Supervision, Methodology, Investigation, Funding acquisition, Formal analysis, Data curation.

Declaration of competing interest

The authors declare that they have no known competing financial interests or personal relationships that could have appeared to influence the work reported in this paper.

Acknowledgment

A.P.P., L.D. and E.D.B. acknowledged the PRIN-2022 project-Prot.2022ZWYSKY "Advanced materials for reversible solid oxide cells" (AMARILLO) CUP E53D23005370006 of the Italian Ministry for University and Research (MUR) funded by the European UnionNext Generation EU.

J.B.F. and E.F. acknowledged the funding from the Swiss National Science Foundation through its PRIMA grant (grant no. PR00P2_193111).

We acknowledge the Paul Scherrer Institute (Villigen, Switzerland) for providing beamtime at the *Phoenix* beamline of the Swiss Light Source (SLS).

Appendix A. Supplementary data

Supplementary data to this article can be found online at https://doi.org/10.1016/j.apsusc.2026.166536.

References

[1] M.B. Hossain, M.R. Islam, K.M. Muttaqi, D. Sutanto, A.P. Agalgaonkar, Advancement of fuel cells and electrolyzers technologies and their applications to renewable-rich power grids, J. Storage Mater. 62 (2023) 106842.
[2] W.T. Hong, M. Risch, K.A. Stoerzinger, A. Grimaud, J. Suntivich, Y. Shao-Horn, Toward the rational design of non-precious transition metal oxides for oxygen electrocatalysis, Energ. Environ. Sci. 8 (2015) 1404–1427.
[3] T. Sadhasivam, K. Dhanabalan, S.-H. Roh, T.-H. Kim, K.-W. Park, S. Jung, M. D. Kurkuri, H.-Y. Jung, A comprehensive review on unitized regenerative fuel cells: crucial challenges and developments, Int. J. Hydrogen Energy 42 (2017) 4415–4433.
[4] A. Maletzko, E.G. Villa, B. Kintzel, H. Fietzek, G. Schmidt, J. Christen, P. Veit, P. Kühne, A. Bornet, M. Arenz, Catalyst interaction in unitized regenerative fuel cells, J. Electrochem. Soc. 171 (2024) 054523.
[5] C.E. Beall, E. Fabbri, T.J. Schmidt, Perovskite oxide based electrodes for the oxygen reduction and evolution reactions: the underlying mechanism, ACS Catal. 11 (2021) 3094–3114.
[6] D.F. Abbott, E. Fabbri, M. Borlaf, F. Bozza, R. Schäublin, M. Nachtegaal, T. Graule, T.J. Schmidt, Operando X-ray absorption investigations into the role of Fe in the electrochemical stability and oxygen evolution activity of Ni1–xFexOy nanoparticles, J. Mater. Chem. A 6 (2018) 24534–24549.
[7] Y. Wang, D. Wang, Y. Li, A fundamental comprehension and recent progress in advanced Pt-based ORR nanocatalysts, SmartMat 2 (2021) 56–75.

[8] J. Guo, A. Hsu, D. Chu, R. Chen, Improving oxygen reduction reaction activities on carbon-supported Ag nanoparticles in alkaline solutions, J. Phys. Chem. C 114 (2010) 4324–4330.
[9] H. Osgood, S.V. Devaguptapu, H. Xu, J. Cho, G. Wu, Transition metal (Fe, Co, Ni, and Mn) oxides for oxygen reduction and evolution bifunctional catalysts in alkaline medi, Nano Today 11 (2016) 601–625.
[10] C. Sun, J.A. Alonso, J. Bian, Recent advances in perovskite-type oxides for energy conversion and storage applications, Adv. Energy Mater. 11 (2021) 2000459.
[11] S. Gupta, W. Kellogg, H. Xu, X. Liu, J. Cho, G. Wu, Bifunctional perovskite oxide catalysts for oxygen reduction and evolution in alkaline media, Chem.–an Asian J. 11 (2016) 10–21.
[12] M.B. Hanif, M. Motola, S. Rauf, C.-J. Li, C.-X. Li, Recent advancements, doping strategies and the future perspective of perovskite-based solid oxide fuel cells for energy conversion, Chem. Eng. J. 428 (2022) 132603.
[13] J. Sunarso, S.S. Hashim, N. Zhu, W. Zhou, Perovskite oxides applications in high temperature oxygen separation, solid oxide fuel cell and membrane reactor: a review, Prog. Energy Combust. Sci. 61 (2017) 57–77.
[14] H. Wang, M. Zhou, P. Choudhury, H. Luo, Perovskite oxides as bifunctional oxygen electrocatalysts for oxygen evolution/reduction reactions–a mini review, Appl. Mater. Today 16 (2019) 56–71.
[15] E. Fabbri, A. Habereder, K. Waltar, R. Kötz, T.J. Schmidt, Developments and perspectives of oxide-based catalysts for the oxygen evolution reaction, Cat. Sci. Technol. 4 (2014) 3800–3821.
[16] J. Suntivich, H.A. Gasteiger, N. Yabuuchi, H. Nakanishi, J.B. Goodenough, Y. Shao-Horn, Design principles for oxygen-reduction activity on perovskite oxide catalysts for fuel cells and metal–air batteries, Nat. Chem. 3 (2011) 546–550.
[17] J. Suntivich, K.J. May, H.A. Gasteiger, J.B. Goodenough, Y. Shao-Horn, A perovskite oxide optimized for oxygen evolution catalysis from molecular orbital principles, Science 334 (2011) 1383–1385.
[18] H. Lee, O. Gwon, K. Choi, L. Zhang, J. Zhou, J. Park, J.-W. Yoo, J.-Q. Wang, J. H. Lee, G. Kim, Enhancing bifunctional electrocatalytic activities via metal d-band center lift induced by oxygen vacancy on the subsurface of perovskites, ACS Catal. 10 (2020) 4664–4670.
[19] S. She, J. Yu, W. Tang, Y. Zhu, Y. Chen, J. Sunarso, W. Zhou, Z. Shao, Systematic study of oxygen evolution activity and stability on La1−xSrxFeO3−δ perovskite electrocatalysts in alkaline media, ACS Appl. Mater. Interfaces 10 (2018) 11715–11721.
[20] Z. Shen, Y. Zhuang, W. Li, X. Huang, F.E. Oropeza, E.J. Hensen, J.P. Hofmann, M. Cui, A. Tadich, D. Qi, Increased activity in the oxygen evolution reaction by Fe4+-induced hole states in perovskite La1–xSrxFeO3, J. Mater. Chem. A 8 (2020) 4407–4415.
[21] S. Ingavale, M. Gopalakrishnan, C.M. Enoch, C. Pornrungroj, M. Rittiruam, S. Praserthdam, A. Somwangthanaroj, K. Nootong, R. Pornprasertsuk, S. Kheawhom, Strategic design and insights into lanthanum and strontium perovskite oxides for oxygen reduction and oxygen evolution reactions, Small 20 (2024) 2308443.
[22] F.H. Taylor, J. Buckeridge, C.R.A. Catlow, Screening divalent metals for A-and B-site dopants in LaFeO3, Chem. Mater. 29 (2017) 8147–8157.
[23] D. Neagu, G. Tsekouras, D.N. Miller, H. Ménard, J.T. Irvine, In situ growth of nanoparticles through control of non-stoichiometry, Nat. Chem. 5 (2013) 916–923.
[24] D. Neagu, V. Kyriakou, I.-L. Roiban, M. Aouine, C. Tang, A. Caravaca, K. Kousi, I. Schreur-Piet, I.S. Metcalfe, P. Vernoux, In situ observation of nanoparticle exsolution from perovskite oxides: from atomic scale mechanistic insight to nanostructure tailoring, ACS Nano 13 (2019) 12996–13005.
[25] O. Kwon, S. Joo, S. Choi, S. Sengodan, G. Kim, Review on exsolution and its driving forces in perovskites, J. Phys.: Energy 2 (2020) 032001.
[26] L. Thommy, O. Joubert, J. Hamon, M.-T. Caldes, Impregnation versus exsolution: using metal catalysts to improve electrocatalytic properties of LSCM-based anodes operating at 600 C, Int. J. Hydrogen Energy 41 (2016) 14207–14216.
[27] E. Vera, V. Trillaud, J. Metaouaa, M. Aouine, A. Boreave, L. Burel, I.-L. Roiban, P. Steyer, P. Vernoux, Comparative study of exsolved and impregnated Ni nanoparticles supported on nanoporous perovskites for low-temperature CO oxidation, ACS Appl. Mater. Interfaces 16 (2024) 7219–7231.
[28] J. Lee, M. Bae, J. Bae, Effects of preparation method on exsolution and alloy formation in a PtRu bimetallic catalyst for hydrogen production via diesel reforming: Impregnation versus combustion synthesis, Int. J. Hydrogen Energy 47 (2022) 29327–29336.
[29] Y. Wang, Z. Wang, C. Jin, C. Li, X. Li, Y. Li, R. Yang, M. Liu, Enhanced overall water electrolysis on a bifunctional perovskite oxide through interfacial engineering, Electrochim. Acta 318 (2019) 120–129.
[30] G. Han, M. Zhuansun, T. Wang, Y. Wang, B-site-metal exsolution on perovskite oxides activates alkaline water oxidation via the lattice oxygen mechanism, Adv. Mater. Interfaces 11 (2024) 2300760.
[31] Y. Jiang, Z. Geng, Y. Sun, X. Wang, K. Huang, Y. Cong, F. Shi, Y. Wang, W. Zhang, S. Feng, Highly efficient B-Site exsolution assisted by Co doping in lanthanum ferrite toward high-performance electrocatalysts for oxygen evolution and oxygen reduction, ACS Sustain. Chem. Eng. 8 (2019) 302–310.
[32] J. Ma, Z. Geng, Y. Jiang, X. Hou, X. Ge, Z. Wang, K. Huang, W. Zhang, S. Feng, Exsolution manipulated local surface cobalt/iron alloying and dealloying conversion in La0·95Fe0·8Co0·2O3 perovskite for oxygen evolution reaction, J. Alloy. Compd. 854 (2021) 157154.
[33] K. Kousi, C. Tang, I.S. Metcalfe, D. Neagu, Emergence and future of exsolved materials, Small 17 (2021) 2006479.
[34] A.P. Panunzi, L. Duranti, I. Luisetto, N. Lisi, M. Marelli, E. Di Bartolomeo, Triggering electrode multi-catalytic activity for reversible symmetric solid oxide cells by Pt-doping lanthanum strontium ferrite, Chem. Eng. J. 471 (2023) 144448.
[35] A.P. Panunzi, L. Duranti, U. Draz, S. Licoccia, C. D'Ottavi, E. Di Bartolomeo, Improved surface activity of lanthanum ferrite perovskite oxide through controlled Pt-doping for solid oxide cell (SOC) electrodes, Ceram. Int. 50 (2024) 31442–31450.
[36] M. Marasi, A.P. Panunzi, L. Duranti, N. Lisi, E. Di Bartolomeo, Enhancing oxygen reduction activity and structural stability of La0.6Sr0.4FeO3−δ by 1 mol% Pt and Ru B-site doping for application in all-perovskite IT-SOFCs, ACS Appl. Energy Mater. 5 (2022) 2918–2928.
[37] S. Ozkan, S.J. Kim, D.N. Miller, J.T. Irvine, A new approach to fuel cell electrodes: lanthanum aluminate yielding fine Pt nanoparticle exsolution for oxygen reduction reaction, Adv. Energy Mater. 14 (2024) 2303025.
[38] W. Li, Y. Zhu, W. Guo, H. Xu, C. Gong, G. Xue, Enhanced oxygen and hydrogen evolution activities of Pt/LaCoO3 perovskite oxide via in-situ exsolution of Pt nanoparticles, J. Chem. Sci. 134 (2022) 38.
[39] J. Wang, J. Yang, A.K. Opitz, W. Bowman, R. Bliem, G. Dimitrakopoulos, A. Nenning, I. Waluyo, A. Hunt, J.-J. Gallet, Tuning point defects by elastic strain modulates nanoparticle exsolution on perovskite oxides, Chem. Mater. 33 (2021) 5021–5034.
[40] T. Götsch, L. Schlicker, M.F. Bekheet, A. Doran, M. Grünbacher, C. Praty, M. Tada, H. Matsui, N. Ishiguro, A. Gurlo, Structural investigations of La0.6Sr0.4FeO3−δ under reducing conditions: kinetic and thermodynamic limitations for phase transformations and iron exsolution phenomena, RSC Adv. 8 (2018) 3120–3131.
[41] E.J. Crumlin, E. Mutoro, W.T. Hong, M.D. Biegalski, H.M. Christen, Z. Liu, H. Bluhm, Y. Shao-Horn, In situ ambient pressure X-ray photoelectron spectroscopy of cobalt perovskite surfaces under cathodic polarization at high temperatures, J. Phys. Chem. C 117 (2013) 16087–16094.
[42] J. Zhu, H. Li, L. Zhong, P. Xiao, X. Xu, X. Yang, Z. Zhao, J. Li, Perovskite oxides: preparation, characterizations, and applications in heterogeneous catalysis, ACS Catal. 4 (2014) 2917–2940.
[43] A. López-García, A.J. Carrillo, C.E. Jiménez, R.S. Anzorena, R. Garcia-Diez, V. Pérez-Dieste, I.J. Villar-Garcia, A.B. Hungría, M. Bär, J.M. Serra, Understanding the evolution of ternary alloyed nanoparticles during reversible exsolution from double perovskite oxides, J. Mater. Chem. A 12 (2024) 22609–22626.
[44] Y. Wang, P. Paciok, L. Pielsticker, W. Wang, A. Spriewald Luciano, M. Ding, L. Glatthaar, W. Hetaba, Y. Guo, J. Gallego, Microscopic insight into ruthenium exsolution from LaFe0.9Ru0.1O3 perovskite, Chem. Mater. (2024) 6246–6256.
[45] A. Bisht, P. Zhang, C. Shivakumara, S. Sharma, Pt-doped and Pt-supported La1–xSrxCoO3: comparative activity of Pt4+ and Pt0 toward the CO poisoning effect in formic acid and methanol electro-oxidation, J. Phys. Chem. C 119 (2015) 14126–14134.
[46] D. Akagi, T. Okato, K. Ishikawa, M. Hori, Low-temperature atomic layer etching of platinum via sequential wet-like reactions of plasma oxidation and complexation, Appl. Surf. Sci. 687 (2025) 162325.
[47] E.G. Sogut, H. Acidereli, E. Kuyuldar, Y. Karatas, M. Gulcan, F. Sen, Single-walled carbon nanotube supported Pt-Ru bimetallic superb nanocatalyst for the hydrogen generation from the methanolysis of methylamine-borane at mild conditions, Sci. Rep. 9 (2019) 15724.
[48] H. Göksu, K. Cellat, F. Şen, Single-walled carbon nanotube supported PtNi nanoparticles (PtNi@ SWCNT) catalyzed oxidation of benzyl alcohols to the benzaldehyde derivatives in oxygen atmosphere, Sci. Rep. 10 (2020) 9656.
[49] https://www.xpsfitting.com/2012/01/platinum.html, pp. X-ray Photoelectron Spectroscopy (XPS) Reference Pages.
[50] https://xpsdatabase.net/platinum-spectra-pto2, pp. XPS database.
[51] Y. Inoue, Y. Miyahara, K. Miyazaki, C. Lee, R. Sakamoto, T. Abe, Tracking activity behavior of oxygen evolution reaction on perovskite oxides in alkaline solution via 3-dimensional electrochemical impedance spectroscopy, J. Electroanal. Chem. 962 (2024) 118270.
[52] K. Zhu, F. Shi, X. Zhu, W. Yang, The roles of oxygen vacancies in electrocatalytic oxygen evolution reaction, Nano Energy 73 (2020) 104761.
[53] E. Marelli, J. Gazquez, E. Poghosyan, E. Müller, D.J. Gawryluk, E. Pomjakushina, D. Sheptyakov, C. Piamonteze, D. Aegerter, T.J. Schmidt, Correlation between oxygen vacancies and oxygen evolution reaction activity for a model electrode: PrBaCo2O5+ δ, Angew. Chem. Int. Ed. 60 (2021) 14609–14619.
[54] B. Ruiz-Camacho, J.B. Vera, A. Medina-Ramírez, R. Fuentes-Ramírez, G. Carreño-Aguilera, EIS analysis of oxygen reduction reaction of Pt supported on different substrates, Int. J. Hydrogen Energy 42 (2017) 30364–30373.
[55] T.H. Wan, M. Saccoccio, C. Chen, F. Ciucci, Influence of the discretization methods on the distribution of relaxation times deconvolution: implementing radial basis functions with DRTtools, Electrochim. Acta 184 (2015) 483–499.
[56] C. Plank, T.G. Bergmann, N. Schlüter, M.A. Danzer, Distribution of relaxation times analysis for impedance spectra containing resistive-inductive characteristics: Part I. Deconvolution methods, J. Electrochem. Soc. 172 (2025) 060514.
[57] H. Schichlein, A.C. Müller, M. Voigts, A. Krügel, E. Ivers-Tiffée, Deconvolution of electrochemical impedance spectra for the identification of electrode reaction mechanisms in solid oxide fuel cells, J. Appl. Electrochem. 32 (2002) 875–882.
[58] M. Ranz, B. Grabner, B. Schweighofer, H. Wegleiter, A. Trattner, Dynamics of anion exchange membrane electrolysis: unravelling loss mechanisms with electrochemical impedance spectroscopy, reference electrodes and distribution of relaxation times, J. Power Sources 605 (2024) 234455.
[59] Y. Lu, C.-Z. Zhao, J.-Q. Huang, Q. Zhang, The timescale identification decoupling complicated kinetic processes in lithium batteries, Joule 6 (2022) 1172–1198.
[60] P. Jiang, Y. Xu, Z. Gong, B. Ge, L. Ding, C. Huang, X. Qiu, Z. Pei, Entropy-driven competitive adsorption sites tailoring unlocks efficient hybrid conversion Zn–air batteries, Angew. Chem. (2025) e202504188.

[61] M. Wu, H. Yuan, H. Zhang, C. Wang, X. Wei, J. Zhu, H. Dai, Analysis of kinetics and operating condition sensitivity for alkaline water electrolyzer by distribution of relaxation times of impedance, J. Power Sources 654 (2025) 237689.
[62] A. Rampf, C. Marchfelder, R. Zeis, Distribution of relaxation times analysis of rotating disk electrode impedance spectra, Electrochim. Acta 514 (2025) 145583.
[63] V.S. Kalimuthu, R. Attias, Y. Tsur, Electrochemical impedance spectra of RuO2 during oxygen evolution reaction studied by the distribution function of relaxation times, Electrochem. Commun. 110 (2020) 106641.
[64] A. Alobaid, C. Wang, R.A. Adomaitis, Mechanism and kinetics of HER and OER on NiFe LDH films in an alkaline electrolyte, J. Electrochem. Soc. 165 (2018) J3395–J3404.
[65] Y. Lu, W. Wang, F. Xie, Investigation of oxygen evolution reaction kinetic process and kinetic parameters on iridium electrode by electrochemistry impedance spectroscopy analysis, J. Electroanal. Chem. 871 (2020) 114281.
[66] G. Pagano, A.P. Panunzi, S. Del Gobbo, N. Lisi, V. Guglielmotti, E. Di Bartolomeo, L. Duranti, Boosting oxygen evolution reaction activity descriptors in LaNiO3 perovskite oxide via one-pot synthesis for alkaline electrolysis, J. Power Sources 663 (2026) 238820.
[67] F.R. Costa, D.V. Franco, L.M. Da Silva, Electrochemical impedance spectroscopy study of the oxygen evolution reaction on a gas-evolving anode composed of lead dioxide microfibers, Electrochim. Acta 90 (2013) 332–343.
[68] A. Kube, W. Strunz, N. Wagner, K.A. Friedrich, Evaluation of electrochemical impedance spectra of-batteries (Li-air/Zn-air) for aqueous electrolytes, Electrochim. Acta 396 (2021) 139261.
[69] E. Sediva, S. Bonizzoni, T. Caielli, P. Mustarelli, Distribution of relaxation times as an accessible method to optimize the electrode structure of anion exchange membrane fuel cells, J. Power Sources 558 (2023) 232608.
[70] Q. Meyer, S. Liu, Y. Li, C. Zhao, Operando detection of oxygen reduction reaction kinetics of Fe–N–C catalysts in proton exchange membrane fuel cells, J. Power Sources 533 (2022) 231058.
[71] T. Götsch, N. Köpfle, M. Grünbacher, J. Bernardi, E.A. Carbonio, M. Hävecker, A. Knop-Gericke, M.F. Bekheet, L. Schlicker, A. Doran, Crystallographic and electronic evolution of lanthanum strontium ferrite (La0.6Sr0.4FeO3−δ) thin film and bulk model systems during iron exsolution, PCCP 21 (2019) 3781–3794.
[72] Q. Lin, Y. Zhu, Z. Hu, Y. Yin, H.-J. Lin, C.-T. Chen, X. Zhang, Z. Shao, H. Wang, Boosting the oxygen evolution catalytic performance of perovskites via optimizing calcination temperature, J. Mater. Chem. A 8 (2020) 6480–6486.
[73] J. Suntivich, W.T. Hong, Y.-L. Lee, J.M. Rondinelli, W. Yang, J.B. Goodenough, B. Dabrowski, J.W. Freeland, Y. Shao-Horn, Estimating hybridization of transition metal and oxygen states in perovskites from Ok-edge x-ray absorption spectroscopy, J. Phys. Chem. C 118 (2014) 1856–1863.
[74] D.N. Mueller, M.L. Machala, H. Bluhm, W.C. Chueh, Redox activity of surface oxygen anions in oxygen-deficient perovskite oxides during electrochemical reactions, Nat. Commun. 6 (2015) 6097.
[75] M. Wang, B. Han, J. Deng, Y. Jiang, M. Zhou, M. Lucero, Y. Wang, Y. Chen, Z. Yang, A.T. N'Diaye, Influence of Fe substitution into LaCoO3 electrocatalysts on oxygen-reduction activity, ACS Appl. Mater. Interfaces 11 (2019) 5682–5686.
[76] F. Frati, M.O. Hunault, F.M. De Groot, Oxygen K-edge X-ray absorption spectra, Chem. Rev. 120 (2020) 4056–4110.
[77] M. Abbate, F.M. de Groot, J. Fuggle, A. Fujimori, O. Strebel, F. Lopez, M. Domke, G. Kaindl, G. Sawatzky, M. Takano, Controlled-valence properties of La1–xSrxFeO3 and La1–xSrxMnO3 studied by soft-x-ray absorption spectroscopy, Phys. Rev. B 46 (1992) 4511.
[78] H. Wadati, A. Chikamatsu, R. Hashimoto, M. Takizawa, H. Kumigashira, A. Fujimori, M. Oshima, M. Lippmaa, M. Kawasaki, H. Koinuma, Temperature-dependent soft X-ray photoemission and absorption studies of charge disproportionation in La1-xSrxFeO3, J. Phys. Soc. Japan 75 (2006) 054704.
[79] A. Braun, D. Bayraktar, S. Erat, A.S. Harvey, D. Beckel, J.A. Purton, P. Holtappels, L.J. Gauckler, T. Graule, Pre-edges in oxygen (1s) x-ray absorption spectra: a spectral indicator for electron hole depletion and transport blocking in iron perovskites, Appl. Phys. Lett. 94 (2009).
[80] J. Wang, J. Yang, A.K. Opitz, D. Kalaev, A. Nenning, E.J. Crumlin, J.T. Sadowski, I. Waluyo, A. Hunt, H.L. Tuller, Strain-dependent surface defect equilibria of mixed ionic-electronic conducting perovskites, Chem. Mater. 34 (2022) 5138–5150.
[81] Y. Guo, S. Wang, R. Li, J. Yu, X. Zhang, M. Li, X. Zheng, J. Zhu, Y. Song, G. Wang, In situ exsolved CoFe alloy nanoparticles for stable anodic methane reforming in solid oxide electrolysis cells, Joule (2024).
[82] N. Hales, J. Huang, B.H. Sjølin, A. Garcia-Padilla, C.N. Borca, T. Huthwelker, I. E. Castelli, R. Skoupy, A.H. Clark, M. Andrzejewski, Confining surface oxygen redox in double perovskites for enhanced oxygen evolution reaction activity and stability, Adv. Energy Mater. (2025) 2404560.
[83] J. Huang, N. Hales, A.H. Clark, N.S. Yüzbasi, C.N. Borca, T. Huthwelker, T. J. Schmidt, E. Fabbri, Operando tracking the interactions between CoOx and CeO2 during oxygen evolution reaction, Adv. Energy Mater. 14 (2024) 2303529.
[84] G.-F. Li, D. Yang, P.-Y. Abel Chuang, Defining nafion ionomer roles for enhancing alkaline oxygen evolution electrocatalysis, ACS Catal. 8 (2018) 11688–11698.